# Probing the Failure Mechanism of SnO$_2$ Nanowires for Sodium-Ion Batteries

Meng Gu,[†] Akihiro Kushima,[‡,§] Yuyan Shao,[⊥] Ji-Guang Zhang,[⊥] Jun Liu,[⊥] Nigel D. Browning,[∥] Ju Li,*[,‡,§] and Chongmin Wang*[,†]

[†]Environmental Molecular Sciences Laboratory, Pacific Northwest National Laboratory, Richland, Washington 99352, United States

[‡]Department of Nuclear Science and Engineering and [§]Department of Materials Science and Engineering, Massachusetts Institute of Technology, 77 Massachusetts Avenue, Cambridge, Massachusetts 02139, United States

[∥]Fundamental and Computational Science Directorate and [⊥]Energy and Environmental Directorate, Pacific Northwest National Laboratory, Richland, Washington 99352, United States

Ⓢ Supporting Information

**ABSTRACT:** Nonlithium metals such as sodium have attracted wide attention as a potential charge carrying ion for rechargeable batteries. Using in situ transmission electron microscopy in combination with density functional theory calculations, we probed the structural and chemical evolution of SnO$_2$ nanowire anodes in Na-ion batteries and compared them quantitatively with results from Li-ion batteries (Huang, J. Y.; et al. *Science* **2010**, *330*, 1515−1520). Upon Na insertion into SnO$_2$, a displacement reaction occurs, leading to the formation of amorphous Na$_x$Sn nanoparticles dispersed in Na$_2$O matrix. With further Na insertion, the Na$_x$Sn crystallized into Na$_{15}$Sn$_4$ ($x$ = 3.75). Upon extraction of Na (desodiation), the Na$_x$Sn transforms to Sn nanoparticles. Associated with the dealloying, pores are found to form, leading to a structure of Sn particles confined in a hollow matrix of Na$_2$O. These pores greatly increase electrical impedance, therefore accounting for the poor cyclability of SnO$_2$. DFT calculations indicate that Na$^+$ diffuses 30 times slower than Li$^+$ in SnO$_2$, in agreement with in situ TEM measurement. Insertion of Na can chemomechanically soften the reaction product to a greater extent than in lithiation. Therefore, in contrast to the lithiation of SnO$_2$ significantly less dislocation plasticity was seen ahead of the sodiation front. This direct comparison of the results from Na and Li highlights the critical role of ionic size and electronic structure of different ionic species on the charge/discharge rate and failure mechanisms in these batteries.

**KEYWORDS:** Na-ion battery, SnO$_2$ anode, in situ TEM, Na diffusion, DFT calculation, failure mechanism
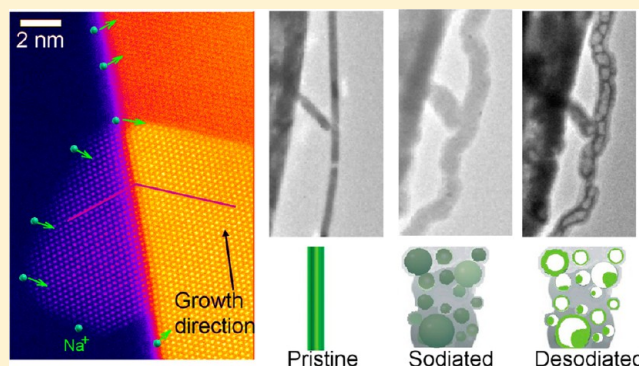
The ever-growing need for high-capacity energy storage in applications ranging from portable electronics, electric vehicles to green energy has spurred the search for new battery concepts beyond Li-ion.[1−10] The Na-ion rechargeable battery is one example of this effort.[11−13] Compared to Li-ion batteries, Na-ion batteries are more cost-effective and sodium is much more earth abundant and environmental friendly.[7,11−13] However, due to its relatively short development history, the fundamental limiting factors and failure mechanisms of the Na-ion batteries remain largely unknown.[7]

In electrochemical terms, there is great similarity between Li-ion and Na-ion batteries, as the Na and Li are adjacent Group 1 elements on the periodic table. The anode materials used in both Li-ion and Na-ion batteries, such as SnO$_2$, Sn, and SnSb alloy, usually undergo huge volume change upon Li/Na insertion and extraction, which requires smart designing concept to accommodate the volume changes for improving the cyclability of the battery.[12,13] Repeated cycling of the anode materials leads to cracks, loss of electric contact, and eventually failure of the battery. To improve battery performance, nanoscale materials are frequently used due to facile stress release and high resistance to structural-defect formations.[14] Nanowires, nanotubes, nanorods, thin films, core−shell nano-materials, and nanocomposites are proposed to improve the capacity and cycling stability of the Li-ion or Na-ion batteries.[12,13,15−25]

Various SnO$_2$ nanostructures, including SnO$_2$ nanorods, SnO$_2$/graphene composites, and carbon-coated mesoporous SnO$_2$ microspheres have emerged as promising anode materials that deliver high-rate and high-capacity in Na-ion batteries.[26,27] It is proposed that SnO$_2$ first reacts with Na to form Na$_x$Sn particles that were embedded inside the Na$_2$O matrix; and with
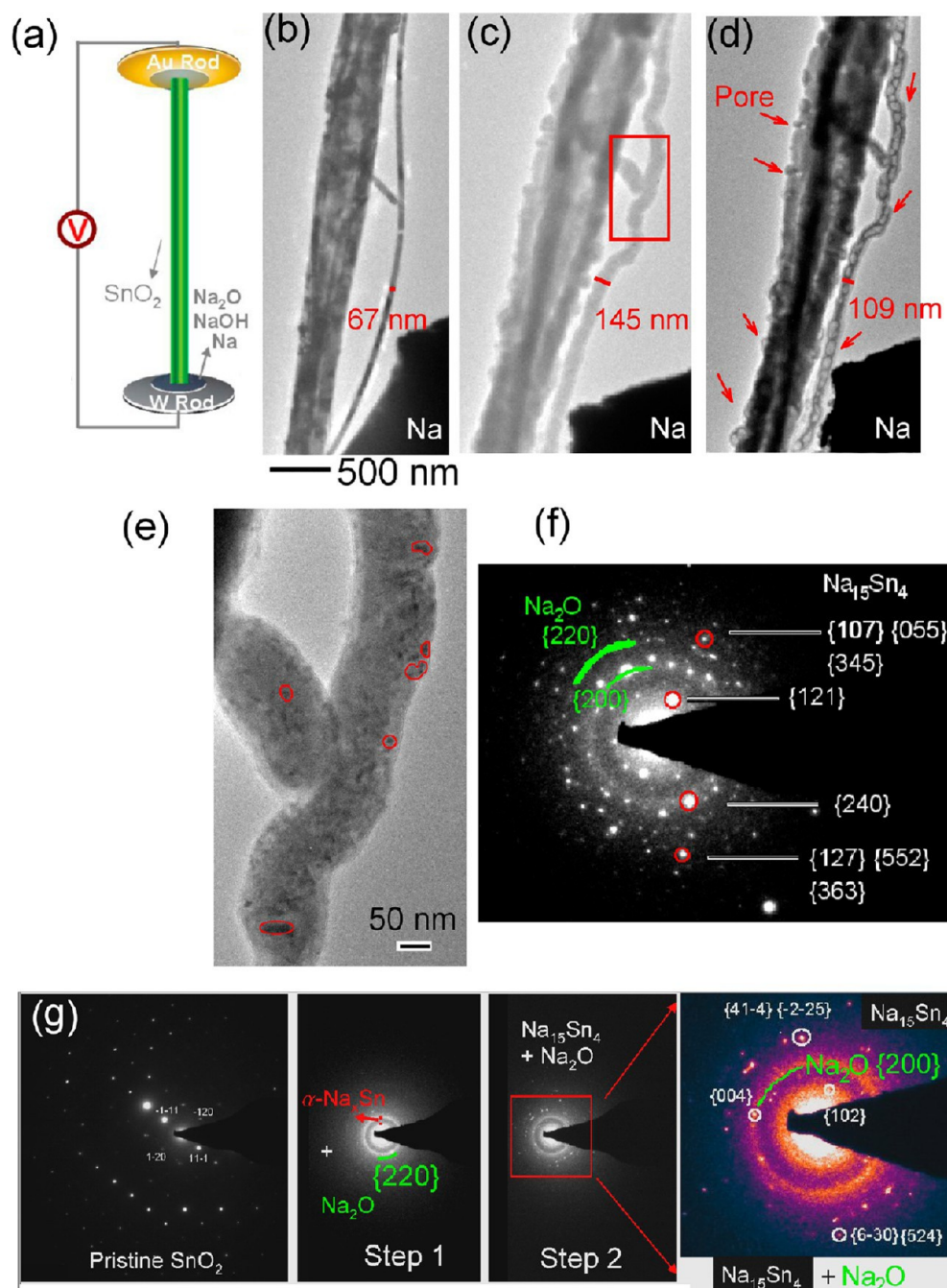
**Figure 1.** (a) Schematic drawing showing the setup of the experiment; TEM images showing (b) pristine $SnO_2$ nanowire; (c) sodiated, and (d) desodiated states of the same nanowire; (e) magnified TEM image of the region marked by the red rectangle in panel (c); (f) electron diffraction pattern after full sodiation; (g) electron diffraction pattern evolution as the sodiation proceeds, diffraction pattern of the pristine $SnO_2$; at sodiation step 1, $\alpha$-$Na_xSn$ (red) and $Na_2O$ (green); at sodiation step2, $Na_{15}Sn_4$ diffraction spots labeled by white circles and $Na_2O$ (green). The scale bar in panel (b) can be applied to the panels (c,d). The red arrows in panel (d) point to the location of the pores following Na extraction.

continued increase of Na in $Na_xSn$, it eventually crystallizes to $Na_{15}Sn_4$.[26,27] But how each phase structurally and chemically evolves during subsequent electrochemical cycling is not clear. In particular, the sodiation characteristics and the failure mechanism of the $SnO_2$-based anode are largely unknown.

In this work, we employed a state-of-the-art in situ transmission electron microscopy (TEM) electrochemical testing technique to directly observe the structural and chemical evolution of $SnO_2$ nanowire upon sodiation/desodiation.[4,22,28−34] In combination with density functional theory (DFT) calculations, we gained fundamental understanding of

the failure mechanism of $SnO_2$ as anode for Na-ion battery. The information gained regarding the dynamic structure changes is used to model the failure mechanism of the battery electrode,[22,29−32] and shows that the same electrode material can respond differently to lithiation and sodiation. The experimental setup for the in situ TEM has been very well documented in previous publications and will only be described briefly here.[28] The nanobattery was assembled onto a Nanofactory TEM scanning tunneling microscopy holder. The Na metal was attached to a W rod, which was loaded on the holder. On the other end, the $SnO_2$ nanowires were welded
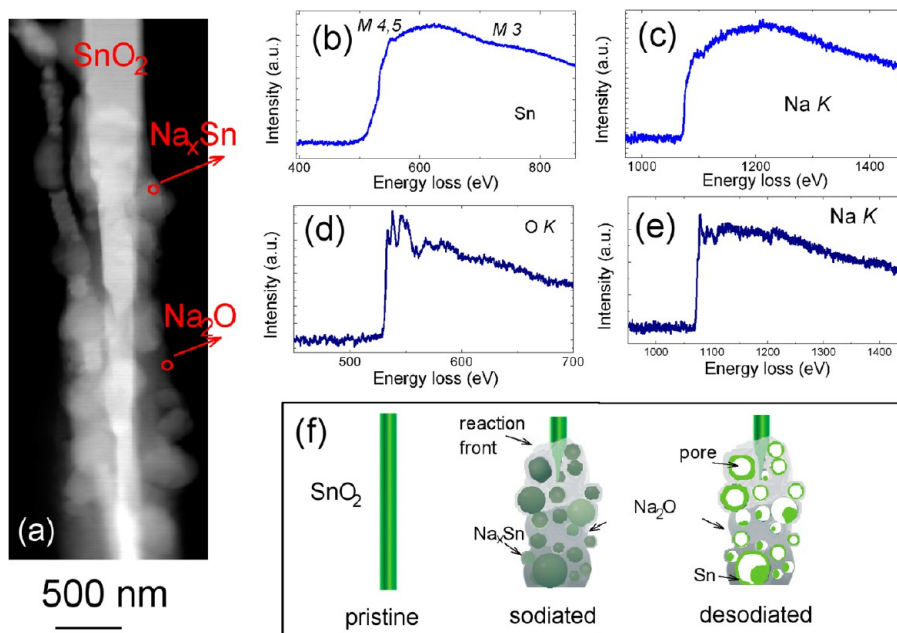
**Figure 2.** (a) STEM Z-contrast image showing the reaction front of the $SnO_2$ nanowire; and STEM-EELS showing: (b) Sn $M$ edge and (c) Na $K$ edges obtained with the electron beam positioned in the particle with a higher brightness in the Z-contrast image; (d) O $K$ edge and (e) Na $K$ edge with the electron beam positioned in the $Na_2O$ matrix region close to the surface, which gives a low brightness in the Z-contrast image; (f) schematic drawing showing the morphology evolution of the $SnO_2$ nanowire upon Na insertion and extraction.

onto a gold rod by conductive epoxy as shown in Figure 1a. The Na metal was loaded on the TEM holder in an Ar-filled glovebox to avoid over oxidation of the Na metal. The loading of the in situ TEM holder into the microscope is performed using a handmade Ar-filled glovebag. During the whole loading procedure, the air exposure of the sample is limited to less than ~2 s. The thin layer of $Na_2O$ and NaOH formed on the Na metal as a result of the short time air exposure serves perfectly as the electrolyte.[33] The $SnO_2$ was sodiated by applying a negative bias of −2 V against the Na metal. During the desodiation, we applied a bias of up to +3 V to drive the $Na^+$ out of the $Na_xSn$. All the in situ electrochemical tests and TEM imaging were conducted on a FEI Titan 80−300 kV scanning/transmission electron microscope (S/TEM) operated at 300 kV.

Microstructural evolution of the $SnO_2$ nanowire upon Na insertion (1st sodiation) is representatively shown in Figure 1b,c and Figure S1 in the Supporting Information. The nanowire swells with the progression of sodiation, which is clearly illustrated by the isolated single nanowire at the right side of the image in Figure 1b,c. As marked in the figures, this nanowire grows from 67 to 145 nm in diameter following full sodiation. Extraction of Na upon desodiation leads to the formation of pores (indicated by the red arrows) and the shrinkage of the nanowire (that nanowire shrinks to 109 nm in diameter after Na extraction) as illustrated in Figure 1d. Detailed structural features of the sodiation process are illustrated by the high-magnification TEM imaging in Figure 1e and the diffraction analysis in Figure 1f,g. Figure 1e is a magnified region marked by the red rectangle in Figure 1c, revealing dark crystalline contrasted particles dispersed in a matrix. Electron diffraction pattern shown in Figure 1f confirms the particular structured particles are $Na_{15}Sn_4$ and the matrix is $Na_2O$ after full sodiation. The crystalline $Na_{15}Sn_4$ particle has a typical domain size of tens of nanometers for the case of the nanowire shown in Figure 1e. However, large single crystalline

$Na_{15}Sn_4$ domain of bigger than 100 nm was also observed during the in situ sodiation experiment as shown by the single crystalline diffraction pattern in Figure S1 in the Supporting Information. The structural phase evolution described above is further confirmed by in situ electron diffraction analysis shown in Figure 1g, illustrating that the electron diffraction pattern evolved from pristine $SnO_2$ to a-$Na_xSn$ and $Na_2O$ in the first step and eventually to a crystalline $Na_{15}Sn_4$ with $Na_2O$ upon full sodiation.

The above structural and diffraction analysis results are further corroborated by the results of in situ STEM Z-contrast imaging and electron energy loss spectroscopy (EELS) as illustrated in Figure 2. The contrast in the Z-contrast image is chemically sensitive, reflecting the local average atomic number. Figure 2a shows the Z-contrast image of the reaction front of a nanowire, featuring the crystalline $SnO_2$ core covered by the sodiated composite. Comparing the average atomic number of $Na_xSn$ and $Na_2O$, $Na_xSn$ will show higher brightness than $Na_2O$. On the basis of the EELS spectra shown in Figure 2b−e, the region with a higher brightness contains mainly Sn and Na, while the region with a minimal brightness shows the dominance of O and Na. It should be noted that the EELS spectra from most regions always contain signals of Sn, O, and Na due to the overlap of the $Na_xSn$ and $Na_2O$ domains along the electron beam direction.

Therefore, as schematically illustrated in Figure 2f, upon $Na^+$ insertion into $SnO_2$, a displacement reaction occurs: $(4 + x)Na^+ + (4 + x)e^- + SnO_2 \rightarrow Na_xSn$ (amorphous) $+ 2Na_2O$, leading to the formation of amorphous $Na_xSn$ particles, which are dispersed in $Na_2O$ matrix. As $x$ reaches the critical value of 3.75, the amorphous $Na_xSn$ transforms to crystalline $Na_{15}Sn_4$. The morphology and spatial correlation of $Na_xSn$ depend on the multiple factors, such as the defects density of the $SnO_2$ nanowire, the shape of the $SnO_2$, and the reaction kinetics. For some nanowires, the $Na_xSn$ coarsens to very large size, leading to an overall morphology of $Na_xSn$ core covered by the
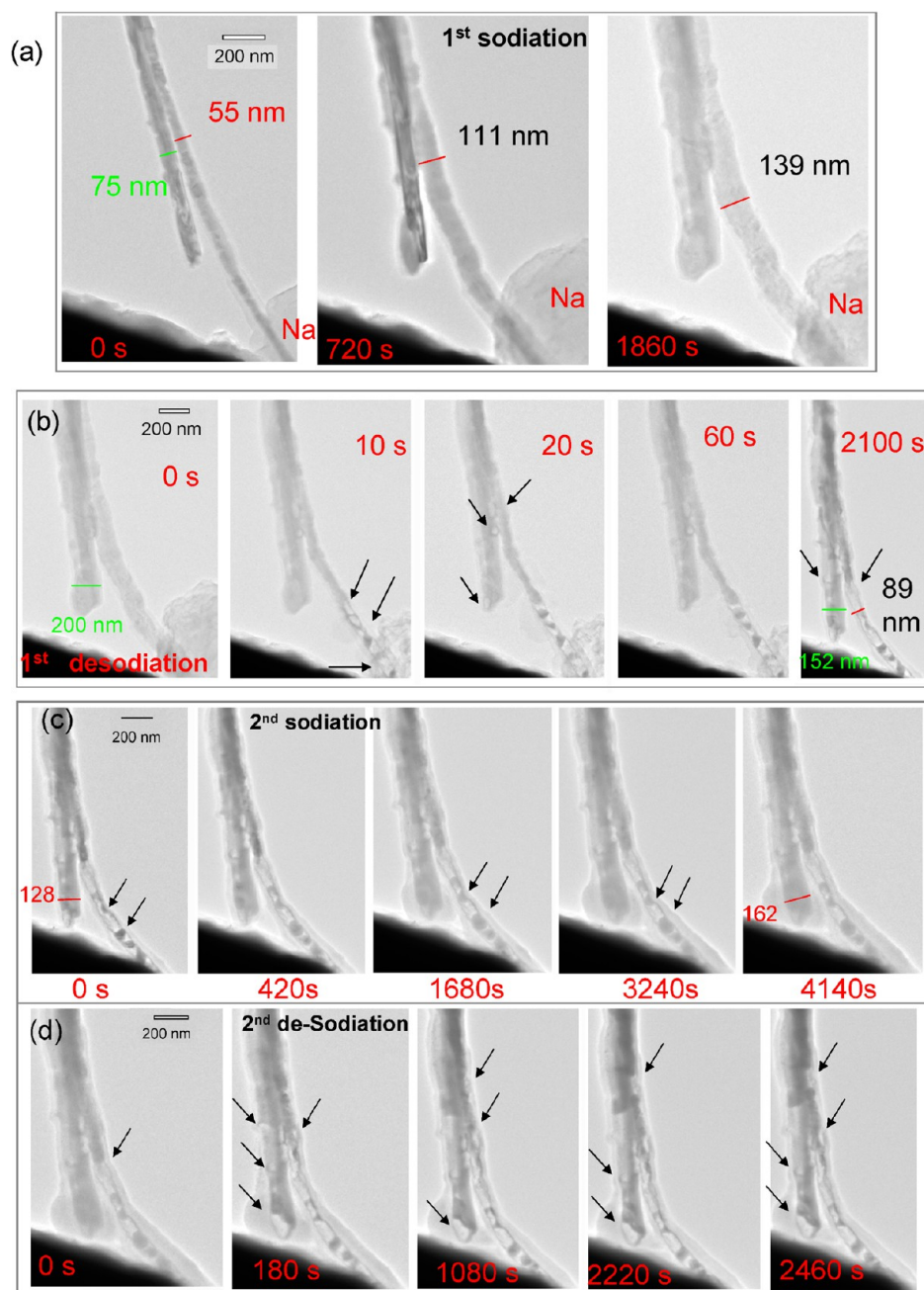
**Figure 3.** TEM images showing the structural evolution of the nanowire during the cyclic sodiation and desodiation: (a) the 1st sodiation, (b) the 1st desodiation, (c) the 2nd sodiation, (d) the 2nd desodiation processes; the black arrows in panels (b) and (d) indicate the pores; the black arrows in panel (c) indicate the limited swelling of the isolated Sn islands.

$Na_2O$ shell as typically illustrated by in situ TEM results shown in Supporting Information Figure S1. It has been noticed that for some nanowires, a significantly thick layer of $Na_2O$ was formed over the whole nanowire as typically shown in Supporting Information Figure S1. The formation of a thin layer of $Na_2O$ on the surface of the nanowire is associated with the fast diffusion of Na spices along the surface of the nanowire, which is the consequence of the nature of the in situ setup of the experiment. However, it appears that the formation of the thick $Na_2O$ surface layer on some nanowires is associated with the effect of the imaging electron beam. Blanking the electron beam or using STEM imaging (low electron dose) as shown in Supporting Information Figure S2 leads to a thinner surface $Na_2O$ layer. Overall, the covering of the whole nanowire by the

$Na_2O$ surface layer will not affect the intrinsic sodiation/desodiation process of the nanowire, but it indeed influences the morphological evolution of the whole nanowire, typically leading to a tapped core−shell sodiation as similarly observed for the case of lithiation.

The morphological evolution shown in Figure 1 and Supporting Information Figure S1 looks quite similar to the Rayleigh−Plateau instability,[35] where a uniform cylinder breaks up into disconnected droplets/particles. We note that ideally, for electrochemical functions, one would like the metallic core in the nanowire to remain a uniform slender cylinder, to enable easy long-range electronic conduction. Unfortunately, a uniform cylinder (e.g., nanowire) is at best metastable with respect to capillary energy variation (if the capillary energy is isotropic,
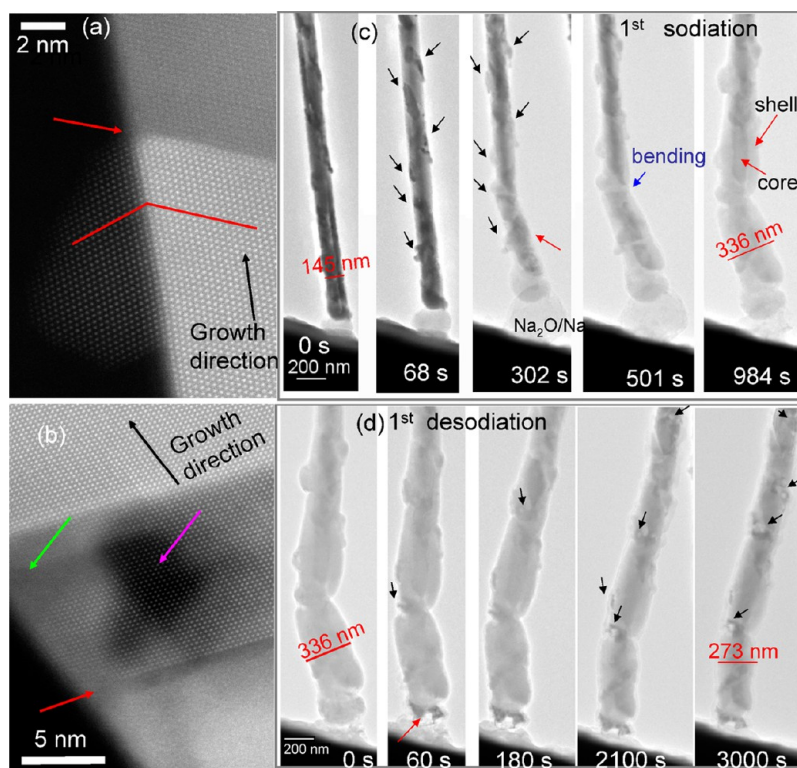
**Figure 4.** (a) STEM Z-contrast image showing the atomic structure of the surface twin grain (marked by the red lines) and the grain boundary structures (red arrow); (b) STEM Z-contrast image showing the grain boundary (red arrow) and associated disordered surface spot (green arrow) and less-dense region with possible void in the z-direction (purple arrow); the growth directions of the nanowires is [011]. TEM images showing (c) the 1st sodiation, (d) the 1st desodiation. Note that the red arrow in the image at 302 s in panel (c) labels the location of the reaction front, while the surface grains begin to sodiate along the whole nanowire; the red arrow in the 60 s image in panel (d) labels a crack formed at the end of the nanowire during desodiation; the black arrows in panel (d) mark the pores formed during desodiation.

then it is unstable as indicated by the Rayleigh−Plateau analysis). At room temperature, such metastability/instability may be "frozen" due to slow diffusion, but the electrochemical cycling activates atomic diffusion, so the breaking up of the cylindrical geometry is perhaps inevitable.

Morphological evolution during the multiple electrochemical cycling process of the $SnO_2$ nanowire is shown in Figure 3. The diameter of the pristine nanowire is 55 nm as labeled by the red line in Figure 3a at 0 s. Upon the initiation of the first sodiation process, the diameter of this nanowire increased from 111 nm at 720 s to 139 nm at 1860 s and formed a composite structure similar to that in Figures 1 and 2. The nanowire at the left of the image in Figure 3 is not directly connected to the Na source. However, the Na$^+$ was transported to the nanowire on the left via the nanowire on the right.. The diameter of the nanowire on the left increased from 75 to 200 nm. During the desodiation, the nanowire on the left shrank from 200 to 152 nm, while the nanowire on the right shrank to 89 nm in diameter compared to the 139 nm after full sodiation (Figure 3b). Most noticeably, formation of pores was observed after 10 s of desodiation as shown by the black arrows in the Figure 3b. The pores expanded in size and extended to the upper region of the nanowire with increasing Na$^+$ extraction as shown by the black arrows in the images at 20 , 60 , and 2100 s. The formation of pores disconnects the metallic constituents of the nanowire, which increases the electrical impedance. Pores are also a form of damage, as they can connect up in bulk electrodes to cause cracking and pulverization. In situ TEM is thus able to provide direct observation of the nucleation and

growth of nanoscopic pores and damage, which would be otherwise quite difficult to obtain.

The second sodiation/desodiation cycle of the nanowire shown in Figure 3a,b is illustrated in Figure 3c,d. The formation of pores greatly limits the electrical conductivity of the isolated Sn islands in the nanowire. In the second sodiation process, most of the Sn islands increased in size by a very limited amount as shown by the black arrow in Figure 3c. The pores were never refilled again in the sodiation process, indicating the disconnected electrical path affects the rechargeable capacity of the Na-ion batteries. In the meantime, the diameter of the nanowire on the left increased from 128 to 162 nm in Figure 3c. During the second desodiation, the pores extended further to the upper region of the right nanowire as shown by the black arrows in the 0−2460 s images in Figure 3d. The pores formed in the nanowire on the left at 180 s are labeled by the black arrows. Finally, the third sodiation process failed (did not happen) due to the disconnected islands by the pores. Therefore, electrical contact played a critical role during the battery cycling. The formation and growth of the pores greatly impacts the electrical connection in the nanowires, resulting in the complete loss of electrochemical cycling capacity of the $SnO_2$ nanowires in the Na-ion batteries. The short cycle life of the nanobattery based on a single nanowire is also partially associated with the nature of the in situ experimental setup. What we observed based on a single nanowire provides insights on the intrinsic response of the material to the Na insertion and extraction, which can be used to guide the designing of composite electrode material for longer cycle life for a real

battery. Therefore, no direct correlation can be made between the short life of single nanowire battery for in situ testing and a real battery electrode. This sodiation characteristic has certain similarity with the degradation mechanism of the Al nanowires as reported by Liu et al. using in situ TEM.[36] Void formation and growth is also observed in the delithiation of the fully lithiated Al nanowire, leading to the breakup of the contiguous Al nanowire to isolated nanoparticles.[36]

Interfaces appear to play an important role in the sodiation process. Some of the $SnO_2$ nanowires were not single crystalline as shown by the atomic-scale Z-contrast images) in Figure 4a,b. Surface twined grains (labeled by red lines) with $(0\bar{1}1)$ mirror plane are observed in pristine $SnO_2$ nanowires in Figure 4a. The contrast in the Z-contrast image can reflect the atomic density in local regions.[9,37] Therefore, disordered surface regions and regions of low density are observed in/close to the grain boundaries as shown in Figure 4b. In the meantime, the surface grains can also be tracked down by the diffraction contrast in conventional TEM images as labeled by the black arrows in the 68 s image in Figure 4c. These surface grains show a darker diffraction contrast due to the orientation difference compared to the bulk of the $SnO_2$ nanowire. At 302 s, the misoriented surface grains were sodiated much faster as compared to the bulk nanowire region. The reaction front of the bulk nanowire is labeled by the red arrow in the image, where the surface $Na_2O$ shell began to form in Figure 4c. The surface grains indicated by the black arrows were noticed to be sodiated preferentially. This likely is related to the faster ion diffusion on the surfaces and along the grain boundaries compared to the bulk crystal region.[38] It is reported that grain boundaries have a lower Li-ion diffusion barrier and provide a faster Li-ion diffusion pathway from experimental measurements and first-principles calculations.[39,40] This observation provides important guidelines for designing high-rate Na-ion batteries through optimization of the microstructure of the electrode, such as by nanocrystallization. In addition, the grain boundaries are weaker in shear and cleavage than the bulk nanowire. Therefore, the expansion of the volume caused by sodiation can break the Sn−O bonds easier in the grain boundaries compared to bulk nanowire region. The fast reaction of the surface grains led to the bending and fracture of the $SnO_2$ nanowire as shown by 501 s image in Figure 4c. The overall diameter of the nanowire finally increased from 145 to 336 nm in the bottom part of the nanowire at 984 s.

The desodiation process of the nanowire in Figure 4d mirrors the results shown in Figure 1d. At 60 s, the swollen section that touched the Na anode cracked as the $Na^+$ was extracted, as indicated by the red arrow in the image at 60 s. With the extraction of $Na^+$ in this sample, pores were also formed as indicated by the black arrows in the images from 60−3000 s. The nanowire shrank from 336 to 273 nm in diameter at the bottom region of the nanowire after 3000 s. The crack and pores formation during the desodiation process negatively impacted the reversible capacity of the $SnO_2$ nanowire for Na-ion batteries.

The second sodiation process of the nanowire shown in Figure 4 is presented in Figure 5a, demonstrating that the $Na^+$ insertion began to fill the pores in the nanowires as labeled by the black arrows in the 0 and 4140 s images in Figure 5a. However, the crack caused by the first desodiation cannot be recovered (compare the 0 and 4140 s image in the location indicated by the red arrows). Thus, the structural damage is irreversible, which is fundamentally the reason for battery
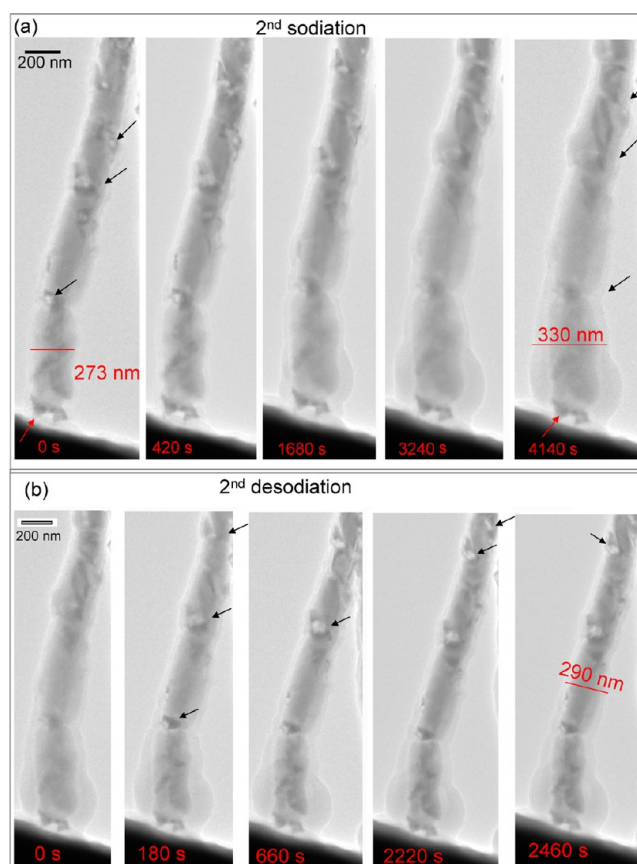


**Figure 5.** TEM images showing (a) the 2nd sodiation, and (b) the 2nd desodiation process. The black arrows indicate the filling of the pores during the 2nd sodiation and formation of the pores again during the 2nd desodiation.

fatigue and failure with electrochemical cycling. The bottom region of the nanowire increased from 273 to 330 nm in diameter as comparing the images taken at 0 and 4140 s. During the second desodiation process as shown in Figure 5b, the pores began to form again as indicated by the black arrows. The diameter of the nanowires shrank back to ∼290 nm in the middle region as labeled in the 2460 s image in Figure 5b.

The diffusion kinetics of $Na^+$ can be inferred based on the location of the reaction front at different times during sodiation as shown in Figure 6. The movement of the reaction front was tracked by following the swelling of the nanowire during sodiation. It can be seen that some small particles formed on the surface of the nanowire shown in Figure 6. These nanosized particles are either $Na_xSn$ or $Na_{15}Sn_4$ in the $Na_2O$ matrix as revealed by electron energy loss spectroscopy and electron diffraction analysis. As shown in Figure 4, these nanowires tend to grow twin grains on the surface of $SnO_2$ nanowires. These twin grains have a larger exposed surface area and were sodiated faster due to fast Na diffusion on the free surface and along grain boundaries, resulting in the formation of particles that appear to be squeezed outside the nanowire surface. The reaction front was labeled by the blue arrows in all the images in Figure 6 and the surface grain labeled by the red arrow in 1470 s was used as a marker to measure the sodiation length. The average sodiation speed is ∼0.56 nm/s based on ∼5 $\mu$m propagation distance shown in Figure 6. The average reaction speed based on Supporting Information Figure S1 is measured to be ∼0.47 nm/s. We also measured the average reaction
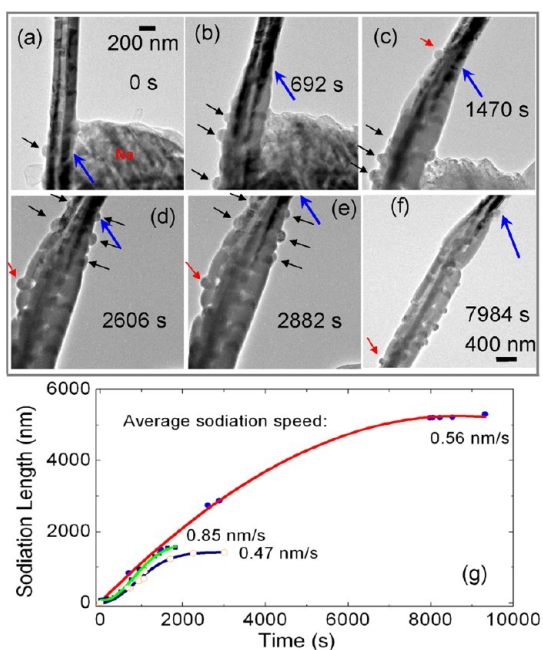
**Figure 6.** (a−f) TEM images of the structural changes and reaction front locations of one nanowire at different times; (g) plotted sodiation length vs time. Note that the blue arrows indicate the location of the reaction fronts in all the TEM images in (a); the red arrows indicate the surface grain used as a marker to calculate the sodiation length; and the scale bar in panel (a) can be applied to (b–e). Note that the red, green, and blue curves in panel (g) are based on the observation in panels a−f, Figure 4(c), and Supporting Information Figure S1(a) respectively.
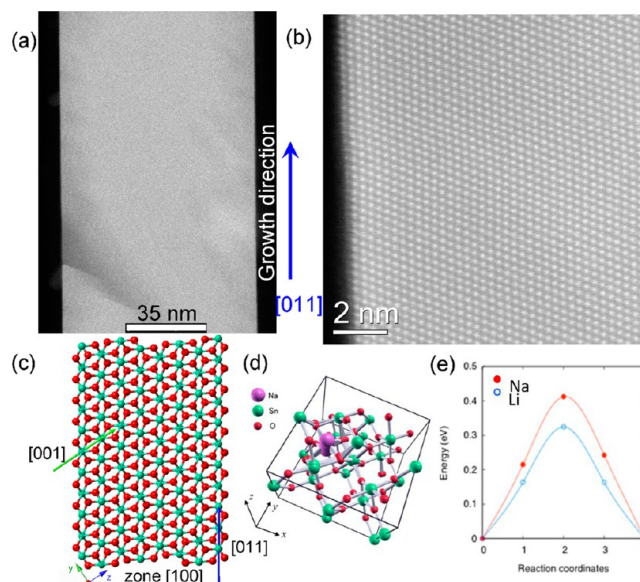


**Figure 7.** (a) Overall view STEM Z-contrast image of the nanowire; (b) atomic scale Z-contrast image of the nanowire; (c) atomic model of the nanowire; (d) calculated diffusion saddle-point configuration of $Na^+$ and $Li^+$ in $SnO_2$ matrix along $[001]$; (e) superposed minimum energy path of the Na/Li migration in $SnO_2$ along $[001]$. x, y, and z correspond to $[100]$, $[010]$, and $[001]$ direction, respectively;.

speed for the nanowire shown in Figure 4, yielding ∼0.85 nm/s. Therefore, all those data statistically give an average reaction speed of ∼0.63 ± 0.2 nm/s as collectively drawn in Figure 6g. The overall reacted length as a function of time follows the rule of parabolic kinetics, indicating a diffusion limited reaction process and similar behavior has been observed for the case of electrochemically driven Li insertion into $SnO_2$.[4] These statistics show that the sodiation process in $SnO_2$ is relatively slower than the lithiation process. For the case of Li into $SnO_2$, the average speed is estimated to be ∼10 nm/s over a similar distance.[4] Thus, lithiation appears to be ∼20 times faster than sodiation. It should be pointed out that the reaction speed measured by the in situ technique for the case of Li into $SnO_2$ is based on ionic liquid electrolyte, while for Na into $SnO_2$, the solid electrolyte ($Na_2O$) is used. Given the fact that the measured reaction speed is a reflection of the intrinsic properties of the $SnO_2$ in response to ionic insertion of either $Li^+$ or $Na^+$, the choice of a different electrolyte would not be expected to affect the measured reaction speed in the solid despite the difference of the overpotential applied for different electrolyte. The experimentally observed differences on the reaction speed of Li and Na into $SnO_2$ are consistently supported by the theoretical considerations as described in the following section.

To gain a fundamental understanding of the migration of Na in $SnO_2$, we acquired atomic resolution Z-contrast images of $SnO_2$ nanowire and calculated the migration energy of Na and Li in $SnO_2$. The overall view and atomic scale Z-contrast image of the $SnO_2$ nanowire in Figure 7a,b showed that the growth direction of the nanowire is along $[011]$ direction and the viewing zone axis is $[100]$ as compared to the atomic model of

the nanowire in Figure 7c. As is found in previous research, the $[001]$ direction (as labeled by the green arrow in Figure 7c) is the fastest and dominant ion diffusion direction in $SnO_2$.[4] Therefore, the energy profile of the Na/Li migration in the $SnO_2$ along $[001]$ is calculated based on the model shown in Figure 7d. The calculated migration barrier was 0.41 eV for Na and 0.32 eV for Li as shown by Figure 7e. This makes the diffusivity of Na in the $SnO_2$ only ∼3% of that of Li at room temperature. The difference in the migration barrier can be attributed to the size of the two ions. In our calculation, the volume expansion was +6.7 $Å^3$ for the $1Li/8SnO_2$ and +9.6 $Å^3$ for the $1Na/8SnO_2$. We thus can say that the Na ion is ∼40% larger in volume than Li in $SnO_2$. During charging of $SnO_2$ nanowires, $Na^+/Li^+$ will most likely receive electrons from the surface of the nanowire as it contacts the electrode surface and becomes Na/Li atom. Therefore, calculation of Na/Li "atom" migration in SnO2 represents the actual migration behavior. Additionally, even though Na/Li atom is considered in our calculations, Na/Li atom will donate electrons to surrounding Sn or O atoms due to its low electronegativity, and it will migrate in the $SnO_2$ in the form of "ions". We performed a Bader charge analysis and confirmed that electron was transferred from Na/Li to oxygens in the system. The DFT result agrees well with the slow propagation of the reaction front during the sodiation (∼0.56 nm/s) as contrasted with 10 nm/s for the case of Li into $SnO_2$.[4]

Another conspicuous difference with the lithiation of $SnO_2$[4] is that while ample dislocation plasticity is observed in crystalline $SnO_2$ ahead of the reaction front, less dislocation cloud can be seen during sodiation in the diffraction-contrast TEM movies S1−S3. Plasticity is driven by the stress generated from the volume change, and it can occur ahead of the chemical reaction front (in the crystalline $SnO_2$), and/or behind the reaction front (in the $Na_xSn$ (amorphous) + $2Na_2O$ composite). In lithiation, plasticity clearly occurs well ahead of the chemical reaction front, but it is hardly evident for the

case of sodiation. To probe why, Figure 8a–b shows the atomic model and tensile stress–strain relations for the $SnO_2$ at
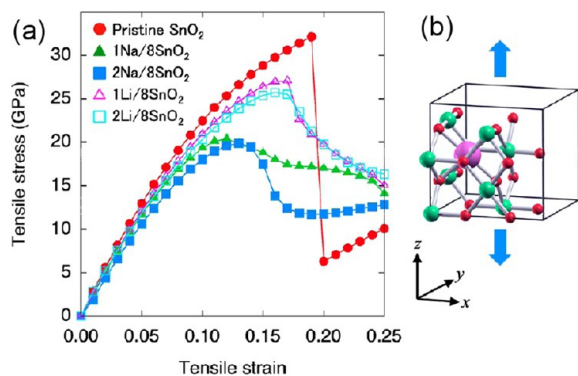


**Figure 8.** (a) Calculated stress–strain curves of the $SnO_2$ (circles), $1Na/8SnO_2$ (filled triangles), $2Na/8SnO_2$ (filled squares), $1Li/8SnO_2$ (open triangles), and $2Li/8SnO_2$ (open squares) along [001]. (b) The atomic structure shown is the simulation cell of the $1Na/8SnO_2$. $x, y$, and $z$ correspond to [100], [010], and [001] direction, respectively.

different Na/Li concentrations. Relatively low concentration of Na/Li in the host $SnO_2$ was considered to simulate the early state of the sodiation/lithiation. The detailed calculation method is given in the Supporting Information. The calculated ideal tensile strength of the pristine $SnO_2$ was 32.1 GPa. It decreased to 20.4 GPa for the $1Na/8SnO_2$ and 19.9 GPa for the $2Na/8SnO_2$ concentration. The reduction of the tensile strength was ∼60%. At the same ratio of Li concentration, the effect on the tensile strength was much smaller and the $SnO_2$ retained 80% of the strength at the $2Li/8SnO_2$ concentration. Similarly, the Young's modulus was also significantly affected by Na insertion as contrasted with Li insertion. Specifically, the Young's modulus decreased to 72% (220 GPa) at the $2Na/8SnO_2$ from 294 GPa of the pristine $SnO_2$, while it was 96% (279 GPa) for the $2Li/8SnO_2$. The message from these calculations seems to be that sodiation causes much more significant decrease in the strength, that is, softening, of the reaction product, than lithiation (which is reasonable due to ∼40% larger volume of Na and therefore greater structural disruption). Consequently, plasticity occurs more preferably in the product in/behind the reaction front, than in the unreacted region ahead of the chemical reaction front. We also note that the chemical reaction front in sodiation is less pluglike than in lithiation of $SnO_2$, which alters the stress distribution and condition for plasticity. With the noted differences in ion diffusivity, concentration-dependent modulus, and strength between Li and Na, the observed differences in reaction morphology and microstructure (dislocation cloud or not) is obviously the outcome of a complex chemomechanical problem[41,42] and should await further modeling.

In summary, in situ TEM has been used to directly visualize the sodiation and desodiation processes of $SnO_2$ nanowire anodes. Sodiation of $SnO_2$ nanowires leads to a structure of $Na_xSn$ particles dispersed in the $Na_2O$ matrix with huge amount of volume expansion (with ∼>100% increase in diameter). Fast sodiation is observed in the misoriented surface grains due to the enhanced $Na^+$ transport along the grain boundaries. The sodiation speed is approximately 1/20th of that of lithiation, in good agreement with the calculated larger diffusion barrier of $Na^+$ in $SnO_2$. Desodiation of $Na_xSn$ results in formation of Sn particles surrounded by pores due to

condensation of vacancies from dealloying. The disconnected network of Sn accounts for the eventual capacity fade of the $SnO_2$ nanowires after several cycles. The sodiation front shows less degree of dislocation cloud generation, which appears to be significant for the case of lithiation of $SnO_2$ nanowires. DFT calculations reveal that the Na-insertion softens the reaction product more than Li-insertion, therefore the large volume change and stress are more preferably accommodated in or behind the sodiation interface through plastic flow of the sodiation product. Our study provides important information regarding the sodiation kinetics and damage mechanism of the electrode materials during electrochemical cycling in Na-ion batteries, which can be used to guide the design of high-performance Na-ion batteries through microstructure control.

## ■ ASSOCIATED CONTENT

**ⓢ Supporting Information**

The following content is included: (1) Supporting movies showing the structural evolution of the $SnO_2$ upon Na insertion and extraction and (2) ab initio calculation methods. This material is available free of charge via the Internet at http://pubs.acs.org.

## ■ AUTHOR INFORMATION

**Corresponding Authors**
*E-mail: (J.L.) liju@mit.edu.
*E-mail: (C.W.) Chongmin.wang@pnnl.gov.
**Notes**
The authors declare no competing financial interest.

## ■ ACKNOWLEDGMENTS

## ■ REFERENCES

(1) Yang, Y.; Zheng, G.; Cui. *Energy Environ. Sci.* **2013**, *6* (5), 1552–1558.
(2) Wu, H.; Chan, G.; Choi, J. W.; Ryu, I.; Yao, Y.; McDowell, M. T.; Lee, S. W.; Jackson, A.; Yang, Y.; Hu, L.; Cui, Y. *Nat. Nanotechnol.* **2012**, *7* (5), 310–315.
(3) Liu, N.; Huo, K.; McDowell, M. T.; Zhao, J.; Cui, Y. *Sci. Rep.* **2013**, *3*, 1919.
(4) Huang, J. Y.; Zhong, L.; Wang, C. M.; Sullivan, J. P.; Xu, W.; Zhang, L. Q.; Mao, S. X.; Hudak, N. S.; Liu, X. H.; Subramanian, A.; Fan, H.; Qi, L.; Kushima, A.; Li, J. *Science* **2010**, *330* (6010), 1515–1520.
(5) Nishimura, S.-i.; Kobayashi, G.; Ohoyama, K.; Kanno, R.; Yashima, M.; Yamada, A. *Nat. Mater.* **2008**, *7* (9), 707–711.
(6) Ellis, B. L.; Makahnouk, W. R. M.; Makimura, Y.; Toghill, K.; Nazar, L. F. *Nat. Mater.* **2007**, *6* (10), 749–753.
(7) Palomares, V.; Serras, P.; Villaluenga, I.; Hueso, K. B.; Carretero-Gonzalez, J.; Rojo, T. *Energy Environ. Sci.* **2012**, *5* (3), 5884–5901.
(8) Bruce, P. G.; Freunberger, S. A.; Hardwick, L. J.; Tarascon, J.-M. *Nat. Mater.* **2012**, *11* (1), 19–29.

(9) Gu, M.; Genc, A.; Belharouak, I.; Wang, D.; Amine, K.; Thevuthasan, S.; Baer, D. R.; Zhang, J.-G.; Browning, N. D.; Liu, J.; Wang, C. *Chem. Mater.* **2013**, *25*, 2319−2326.

(10) Gu, M.; Belharouak, I.; Genc, A.; Wang, Z.; Wang, D.; Amine, K.; Gao, F.; Zhou, G.; Thevuthasan, S.; Baer, D. R.; Zhang, J.-G.; Browning, N. D.; Liu, J.; Wang, C. *Nano Lett.* **2012**, *12* (10), 5186−5191.

(11) Qian, J.; Zhou, M.; Cao, Y.; Ai, X.; Yang, H. *Adv. Energy Mater.* **2012**, *2* (4), 410−414.

(12) Qian, J.; Chen, Y.; Wu, L.; Cao, Y.; Ai, X.; Yang, H. *Chem. Commun.* **2012**, *48* (56), 7070−7072.

(13) Xiao, L.; Cao, Y.; Xiao, J.; Wang, W.; Kovarik, L.; Nie, Z.; Liu, J. *Chem. Commun.* **2012**, *48* (27), 3321−3323.

(14) Gao, H. J.; Ji, B. H.; Jager, I. L.; Arzt, E.; Fratzl, P. *Proc. Natl. Acad. Sci. U.S.A.* **2003**, *100* (10), 5597−5600.

(15) Liu, N.; Hu, L.; McDowell, M. T.; Jackson, A.; Cui, Y. *ACS Nano* **2011**, *5* (8), 6487−6493.

(16) Baranchugov, V.; Markevich, E.; Pollak, E.; Salitra, G.; Aurbach, D. *Electrochem. Commun.* **2007**, *9* (4), 796−800.

(17) Szczech, J. R.; Jin, S. *Energy Environ. Sci.* **2011**, *4* (1), 56−72.

(18) Chakrapani, V.; Rusli, F.; Filler, M. A.; Kohl, P. A. *J. Power Sources* **2012**, *205* (0), 433−438.

(19) Qu, J.; Li, H.; Henry, J. J., Jr; Martha, S. K.; Dudney, N. J.; Xu, H.; Chi, M.; Lance, M. J.; Mahurin, S. M.; Besmann, T. M.; Dai, S. *J. Power Sources* **2012**, *198* (0), 312−317.

(20) Fan, R.; Wu, Y.; Li, D.; Yue, M.; Majumdar, A.; Yang, P. *J. Am. Chem. Soc.* **2003**, *125* (18), 5254−5255.

(21) Cui, L.-F.; Hu, L.; Wu, H.; Choi, J. W.; Cui, Y. *J. Electrochem. Soc.* **2011**, *158* (5), A592−A596.

(22) Liu, N.; Wu, H.; McDowell, M. T.; Yao, Y.; Wang, C.; Cui, Y. *Nano Lett.* **2012**, *12* (6), 3315−3321.

(23) McDowell, M. T.; Lee, S. W.; Ryu, I.; Wu, H.; Nix, W. D.; Choi, J. W.; Cui, Y. *Nano Lett.* **2011**, *11* (9), 4018−4025.

(24) Park, M.-H.; Kim, M. G.; Joo, J.; Kim, K.; Kim, J.; Ahn, S.; Cui, Y.; Cho, J. *Nano Lett.* **2009**, *9* (11), 3844−3847.

(25) Chan, C. K.; Peng, H.; Liu, G.; McIlwrath, K.; Zhang, X. F.; Huggins, R. A.; Cui, Y. *Nat. Nanotechnol.* **2008**, *3* (1), 31−35.

(26) Su, D.; Ahn, H.-J.; Wang, G. *Chem. Commun.* **2013**, *49* (30), 3131−3133.

(27) Wang, Y.; Su, D.; Wang, C.; Wang, G. *Electrochem. Commun.* **2013**, *29* (0), 8−11.

(28) Gu, M.; Li, Y.; Li, X.; Hu, S.; Zhang, X.; Xu, W.; Thevuthasan, S.; Baer, D. R.; Zhang, J.-G.; Liu, J.; Wang, C. *ACS Nano* **2012**, *6* (9), 8439−8447.

(29) Liu, X. H.; Zhong, L.; Huang, S.; Mao, S. X.; Zhu, T.; Huang, J. Y. *ACS Nano* **2012**, *6* (2), 1522−1531.

(30) McDowell, M. T.; Ryu, I.; Lee, S. W.; Wang, C.; Nix, W. D.; Cui, Y. *Adv. Mater.* **2012**, *24* (45), 6034−6041.

(31) Liu, X. H.; Huang, J. Y. *Energy Environ. Sci.* **2011**, *4* (10), 3844−3860.

(32) Wang, C.-M.; Li, X.; Wang, Z.; Xu, W.; Liu, J.; Gao, F.; Kovarik, L.; Zhang, J.-G.; Howe, J.; Burton, D. J.; Liu, Z.; Xiao, X.; Thevuthasan, S.; Baer, D. R. *Nano Lett.* **2012**, *12* (3), 1624−1632.

(33) Wang, J. W.; Liu, X. H.; Mao, S. X.; Huang, J. Y. *Nano Lett.* **2012**, *12* (11), 5897−5902.

(34) Miller, D. J.; Proff, C.; Wen, J. G.; Abraham, D. P.; Bareño, J. *Adv. Energy Mater.* **2013**, DOI: 10.1002/aenm.201300015.

(35) Rayleigh, L. *Proc. R. Soc. London* **1879**, *29*, 71−97.

(36) Liu, Y.; Hudak, N. S.; Huber, D. L.; Limmer, S. J.; Sullivan, J. P.; Huang, J. Y. *Nano Lett.* **2011**, *11* (10), 4188−4194.

(37) Gu, M.; Biegalski, M. D.; Christen, H. M.; Song, C.; Dearden, C. R.; Browning, N. D.; Takamura, Y. *J. Mater. Res.* **2012**, *27* (11), 1436−1444.

(38) Tuller, H. L. *Solid State Ionics* **2000**, *131* (1−2), 143−157.

(39) Zhu, X.; Ong, C. S.; Xu, X.; Hu, B.; Shang, J.; Yang, H.; Katlakunta, S.; Liu, Y.; Chen, X.; Pan, L.; Ding, J.; Li, R.-W. *Sci. Rep.* **2013**, *3*, 1084.

(40) Paul, H.; Sylvio, I. *J. Phys: Condens. Mater.* **2003**, *15* (30), R1257.

(41) Liu, X. H.; Liu, Y.; Kushima, A.; Zhang, S. L.; Zhu, T.; Li, J.; Huang, J. Y. *Adv. Energy Mater.* **2012**, *2* (7), 722−741.

(42) Huang, S.; Fan, F.; Li, J.; Zhang, S.; Zhu, T. *Acta Mater.* **2013**, *61* (12), 4354−4364.

**Supporting Information**

# Probing the Failure Mechanism of SnO$_2$ Nanowires for Sodium-ion Batteries

Meng Gu[1], Akihiro Kushima[2], Yuyan Shao[3], Ji-Guang Zhang[3], Jun Liu[4], Nigel D. Browning[3], Ju Li[2*], and Chongmin Wang[1*]

[1] Environmental Molecular Sciences Laboratory, Pacific Northwest National Laboratory, Richland, WA 99352, USA

[2] Department of Nuclear Science and Engineering and Department of Materials Science and Engineering, Massachusetts Institute of Technology, 77 Massachusetts Avenue, Cambridge, MA 02139

[3] Fundamental and Computational Science Directorate, Pacific Northwest National Laboratory, Richland, WA 99352, USA

[4] Energy and Environmental Directorate, Pacific Northwest National Laboratory, Richland, WA 99352, USA

Authors to whom all correspond should be addressed: liju@mit.edu; Chongmin.wang@pnnl.gov

**The supporting information includes the following content:**

**1: Supporting movie showing the structural evolution of the SnO$_2$ upon Na insertion and extraction**

(1) Movie S1(a):  1$^{st}$ time sodiation of nanowire #1 corresponds to the Fig S1(a)

(2) Movie S1(b):  1$^{st}$ time desodiation of nanowire #1 corresponds to Fig S1(b)

(3) Movie S2(a):  1$^{st}$  time sodiation of nanowire #2, #3 corresponds to Fig 2(a), Fig 3(c)

(4) Movie S2(b):  1$^{st}$ time desodiation of nanowire #2, #3 corresponds to Fig 2(b), Fig3(d)

(5) Movie S2(c):  2$^{nd}$ time sodiation of nanowire #2, #3 corresponds to Fig 2(c), Fig 4(a)

(6) Movie S2(d): 2nd time desodiation of nanowire #2, #3 corresponds to Fig 2(d), Fig 4(b)

(7) Movie S3: 1st time sodiation of nanowire #4 corresponds to Fig 5 (a)

**2: *Ab initio* calculations methods:**

For the tensile simulation of the $SnO_2$, a 6.75 Å × 6.75 Å × 6.45 Å supercell of rutile $SnO_2$ including 8 Sn and 16 O atoms was used. The crystallographic orientations of the simulation cell are [110], [1$\bar{1}$0], and [001] in $x$, $y$, and, $z$ direction, respectively. We employed density functional theory formalism with generalized gradient approximation parameterized by Perdew, Burke and Ernzerhof[1] using planewave basis set. The ionic cores were represented with projector-augmented wave potentials.[2,3] An energy cutoff of 400 eV was chosen for the expansion of the plane wave function and a 4 × 4 × 4 Monkhorst-Pack[4] $k$-point mesh was selected. First, the atomic configurations and the cell vectors were relaxed to minimize the total energy of the single crystal $SnO_2$ system. Then the tensile strain was applied to the model by elongating the simulation cell along $z$ direction with the increment of 0.01. After the each increment of the strain, the structural optimization was performed while fixing the cell size in $z$ direction. Two different Na concentration ratios were considered ($1Na/8SnO_2$ and $2Na/8SnO_2$). The Na atoms were added to the $SnO_2$ at the octahedral interstitial sites, and the Na atoms were placed as far away as possible to each other for $2Na/8SnO_2$ model. We followed the same procedure for the Li insertion to compare the effect of Na and Li on the mechanical property of the $SnO_2$. The simulation was performed using Vienna Ab-initio Simulation Package (VASP).[5,6]

For the calculation of the Na and Li migration in the $SnO_2$, a 9.54 Å × 9.54 Å × 6.45 Å supercell of rutile $SnO_2$ including 16 Sn and 32 O atoms with 1 Na or Li atom inserted to the octahedral site was used. The crystallographic orientations of the simulation cell are [100], [010], and [001] in $x$, $y$, and, $z$ direction, respectively. Once the structural optimization was performed, the migration barrier of Na/Li to the adjacent octahedral site was calculated by the nudged elastic band method.[7] Three images between the initial and the final state were selected in the calculation. Here, we considered the migration along

[001] direction, the dominant path for the Li migration in the rutile $SnO_2$.[8] All the other conditions were same as in the tensile simulation.

**3: Additional Figures to illustrate the possible electron beam effect on the surface Na2O layer development:**

A thick $Na_2O$ surface layer grew due to three reasons: (1) the reaction of $Na^+$ ions with the oxygen ions from the $SnO_2$ nanowire, which is related to fast surface diffusion of Na species, (2) electron beam induced thickening of $Na_2O$ surface layer. To illustrate the electron beam effect on the surface $Na_2O$ layer, we show one image (Figure S2), the electron beam was blanked during the sodiation. As a result, the shell layer is much thinner compared to the results shown in Figure S1.
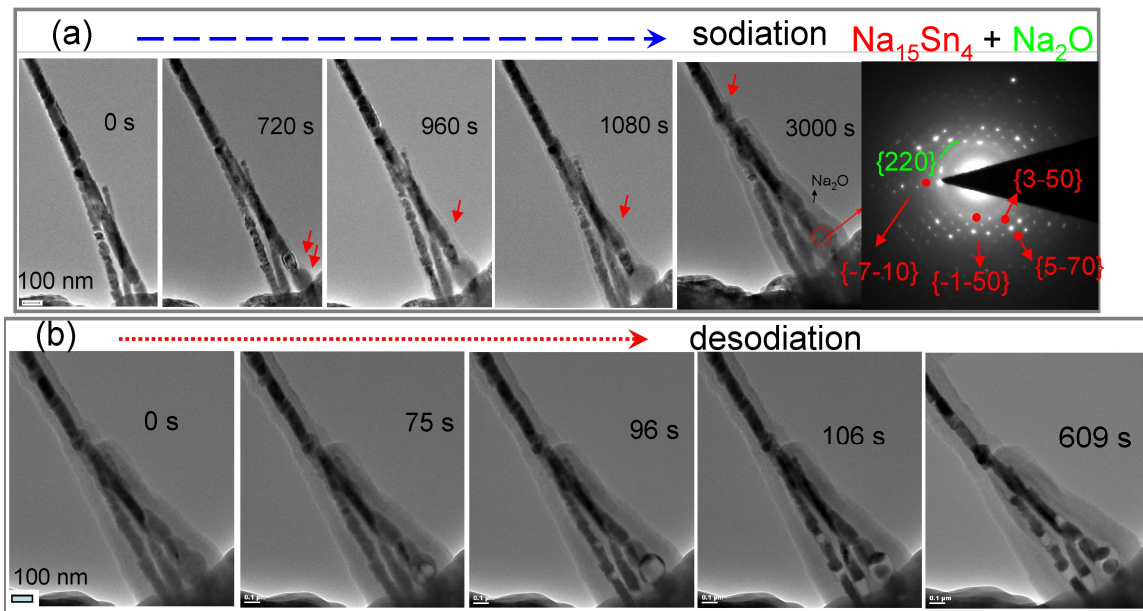


Figure S1 (a) TEM images showing the sodiation process and diffraction pattern at the region circled by red, showing the formation of $Na_{15}Sn_4$ and $Na_2O$ after final sodiation; The diffraction pattern at the very right of the panel (a) shows the formation of $Na_{15}Sn_4$ core (red) and $Na_2O$ (green) shell; and the red arrows label the location of the reaction fronts; (b) desodiation process at different times; The formation of $Na_2O$ surface layer is the consequence of sodiation of $SnO_2$ and electron beam induced surface growth of Na species;
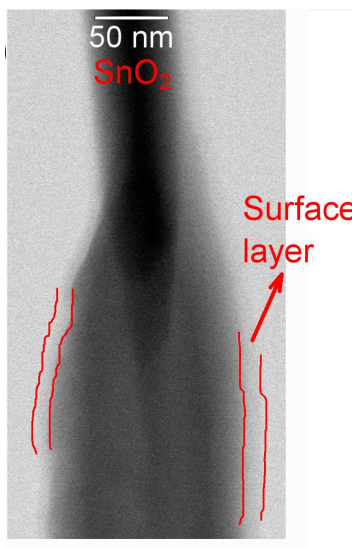
Figure S2 bright-field STEM image of the reaction front with the electron beam being blanked, showing much thinner $Na_2O$ surface layer compared to Figure S1

## References

[1] J.P. Perdew, K. Burke, and M. Ernzerhof, Phys. Rev. Lett. **77**, 3865 (1996).

[2] G. Kresse and D. Joubert, Phys. Rev. B **59**, 1758 (1999).

[3] P.E. Blechel, Phys. Rev. B **50**, 17953 (1994).

[4] H.J. Monkhorst and J.D. Pack, Phys. Rev. B **13**, 5188 (1976).

[5] G. Kresse and J. Hafner, Phys. Rev. B **47**, 558 (1993).

[6] G. Kresse and J. Furthm ller, Phys. Rev. B **54**, 11169 (1996).

[7] G. Mills and H. Jónsson, Phys. Rev. Lett. **72**, 1124 (1994).

[8] F.R. Sensato, L. Gracia, A. Beltrán, J. Andrés, and E. Longo, J. Phys. Chem. C **116**, 16127−16137 (2012).

[9] J.Y. Huang, L. Zhong, C.M. Wang, J.P. Sullivan, W. Xu, L.Q. Zhang, S.X. Mao, N.S. Hudak, X.H. Liu, A. Subramanian, H. Fan, L. Qi, A. Kushima, and J. Li, Science **330**, 1515 −1520 (2010).